AUTHOR'S COPY
Journal of Medical Robotics Research, Vol. 3, No. 1 (2018) 1850003 (10 pages)
#.c World Scientific Publishing Company
DOI: 10.1142/S2424905X18500034

MR Safe Robot Assisted Needle Access of the Brain: Preclinical Study

Changhan Jun[a†], Sunghwan Lim[a†], Jean-Paul Wolinsky[c†], Tomas Garzon-Muvdi[b], Doru Petrisor[a], Kevin Cleary[d], Dan Stoianovici[a*]

[a]*Robotics Laboratory, Urology Department (http://urobotics.urology.jhu.edu/),*
[b]*Department of Neurosurgery, Johns Hopkins University, Baltimore, MD*
[c]*Department of Neurosurgery, Northwestern University, Chicago, IL*
[d]*Children's National Health System, Washington, DC*
[†]*These authors contributed equally to this work, names listed by alphabetical order*
**E-mail: dss@jhu.edu*

We report the results of preclinical experiments for direct MRI-guided needle interventions in the brain. An MR Safe robot was incorporated into an intraoperative MRI system. Deep regions of the brain simulated in a cranial mockup were targeted with a needle under robotic assistance. The 3D accuracy of in-scanner targeting at an average depth of 95mm was 1.55mm, with no manual corrections.

Keywords: MR Safe robot, neurosurgery, direct MRI guided, intraoperative MRI

1. Introduction

Needle interventions are critical for neurosurgical procedures such as biopsy of intracranial lesions, deep brain stimulation (DBS), ventriculoperitoneal shunting (VP), and laser ablation of the hippocampus, among other procedures. These require accurate and precise targeting of surgical tools in deep regions of the brain.

3D imaging modalities such as computed tomography (CT) and magnetic resonance imaging (MRI) have been incorporated into neurosurgical procedures for image guidance. Image guidance has enabled less invasive surgical corridors and improved localization. Traditional neurosurgical procedures have been dependent on preoperative images. However, the brain matter can shift after the dura is opened and the deformation of brain tissue can cause undetected errors. The use of intraoperative imaging enables the images to be updated at critical points of the operation. Several systems have been developed to assist the surgeon such as the Neuromate [1] and the Minerva [2] robots which use CT guidance. However, CT imaging exposes the patient to radiation and provides substantially inferior soft tissue visualization than MRI.

Robotic systems for MR guidance have also been developed. Masamune et al. reported an MRI compatible needle insertion manipulator for stereotactic neurosurgery in a 0.5T scanner [3]. Comber et al [4] reported the initial developments of an MR compatible pneumatic driven cannula robot. Davies et al. developed the Neurobot [5]. Perhaps the most advanced MR compatible robot thus far is the Neuroarm [6], a highly dexterous robot for surgery.

Imaging directly during the operation remains difficult due to the limited access within the MRI scanner. Commonly, the use of intraoperative MRI requires the movement of the patient in and out of the scanner. The alternative approach is to operate directly within the scanner, under direct MRI guidance. The direct approach, however, requires specialized devices to assist the surgeon. Robotic devices for direct MRI guidance should be small, accurate, safe to operate in the MRI, and should not substantially deteriorate the quality of the images, which collectively represent a challenging engineering task. According to ASTM F2503-13, devices are classified as MR Unsafe, Conditional, and Safe. The MR Safe robots pose no known hazards resulting from exposure to any MR environment, and cause virtually no interference with the imaging. Their structure is made of non-metallic materials and are electricity free [7].

For minimally invasive brain procedures the motion of instruments is restricted through the entry point, requiring robotic devices with Remote Center of Motion (RCM) kinematics [8-10], which places further constraints on the robot design. A recent RCM type robot for direct MR guidance in the brain was reported by Hao Su et al. [11]. The robot is actuated by piezoelectric motors and is MR Conditional. Special control electronics enabled the Signal to Noise Ratio (SNR) loss caused by the device to be reduced to only 13%.

We have previously developed special MR Safe motors based on pneumatic power and optical sensing [12], and several MR Safe robots for urology applications [13-16]. We have also recently reported the development of an RCM type MR-Safe robot and its comprehensive image and accuracy testing [17]. This is a general needle guidance robot that could be applied in many MRI applications. In this study, we report its application to neurosurgery in conjunction with an iMRIS (Minnetonka, MN) intraoperative MR scanner.

JHBMC, MFL-W115, Robotics Laboratory, 5200 Eastern Ave, Baltimore, MD 21224

Currently, no accurate means of direct MRI guidance and operation within the scanner have been applied clinically. A robot to guide such operations would allow surgeons to formulate surgical plans based on most recent images, utilize continuous imaging for immediate feedback, and maintain the operative rhythm by eliminating the common in-out moves of the scanner, operating within the scanner under direct imaging. Since the iMRIS is based on a moveable magnet instead of the classic movable table configuration, it facilitates anesthesiology and surgical setup. Moreover, due to its relatively short bore, it could enable manual access within the scanner to manipulate the needle under robotic assistance, as needed for the proposed novel direct MRI approach.

2. The Robotic System

The robot used in this study is a recently developed pneumatically actuated robot made entirely of non-metallic materials (electricity free). Its kinematics, design, construction, and a comprehensive set of tests were reported in [17]. In summary, MR compatibility tests (ASTM F2503) demonstrated that it is MR Safe to operate in any MR environment; electromagnetic compatibility tests (EMC, IEC 60601-1-2) showed no conduction or radiation of EM emissions; image tests in a Siemens Magnetom Aera scanner showed less than 1% change in SNR and virtually no image deterioration and artifacts due to the presence and motion of the robot during MR image acquisition; and a needle targeting accuracy of 1.9mm at a depth of 100mm. Here, we present the robot configuration, image registration, and navigation for the neurosurgery application.

The robot presents three-degrees of freedom (DoF), 2 DoF used for a parallelogram RCM mechanism to orient a needle-guide and 1 DoF for presetting the depth of needle insertion. The insertion is performed manually through the needle-guide up to the preset depth. For the neurosurgical application in the iMRIS intraoperative scanner, a special needle-guide and needle depth offset component were made for 18G needles. In the previous application [17] the robot was attached to the MR table. For the brain application a new support arm was built to mount the robot directly on the Mayfield head holder (3-point skull fixation device) of the iMRIS scanner. The new support arm comprises 3 degrees of adjustment (DoA) and attaches to the head holder with a Hirth coupling. When unlocked, the arm allows the RCM point to be manually located as needed about the skull. The location is then locked with 3 knobs. The support arm is made of polycarbonate, ultem, polysulfone, and garolite materials.

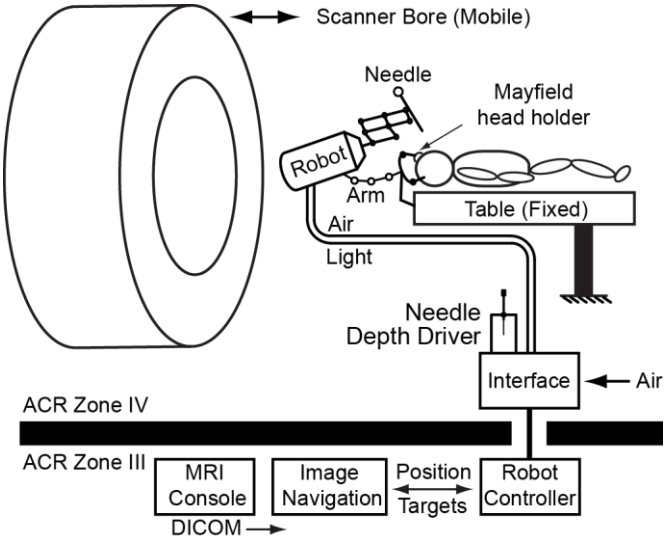

Figure 1: System Configuration

The system is schematically represented in Figure 1. This shows the robot, support arm, and the control components located within and outside the MR room (ACR ZONE IV inside the room with the magnet and ACR ZONE III in the control room).

The robot includes a set of registration markers placed on the RCM structure. A set of MRI coils is placed on the lateral sides of the skull and robot. Images of the markers and brain are acquired simultaneously and transferred over the network in DICOM format to the Image Navigation computer (a Windows 10 PC). Software was developed for image processing and 3D reconstruction, the registration of the robot to the image space, surgical planning, and robot control, needle segmentation, and all other components. The software was written in Visual C++ (Microsoft Corp.) with open source libraries VTK, ITK (Kitware, Albany, NY). In addition to the original software [17], components were developed to improve needle localization in the images with a needle marker.

After initial scanning of the anatomy, target points are selected in the image. The relationship between the image coordinate and the robot coordinate is determined by the registration module. Image coordinates can then be transformed to robot space, further converted to the joint space of the robot through the inverse kinematics, and passed to the motion controller to drive the robot. The robot orients the needle-guide towards the target point. Similarly, the needle depth driver sets the depth of needle insertion that corresponds to the selected target, by positioning an O-ring marker on the needle shaft at the corresponding depth. The surgeon then takes the needle from the driver, and inserts it through the guide up to the marked depth, which should correspond to the needle point being centered on the selected target.

3. Image-to-Robot Registration and Targeting

Image-to-robot registration is an essential procedure for image-guided medical robots. It transforms target points selected in the image space to the robot space. The registration marker comprises four independent linear markers rigidly attached to the top link of the parallelogram RCM structure. The markers are made of glass tubes and filled with Radiance® MRI liquid (Beekley, Bristol, CT). The glass tubes are 6mm outside diameter, 4mm inside diameter, and their lengths are 75mm, 75mm, 45mm, and 28mm. Three of these are arranged in a Z shape (Figure 2) and are used to calculate the actual registration, while the fourth one is placed laterally to facilitate the visual orientation of the Z in the images. The sides of the Z marker

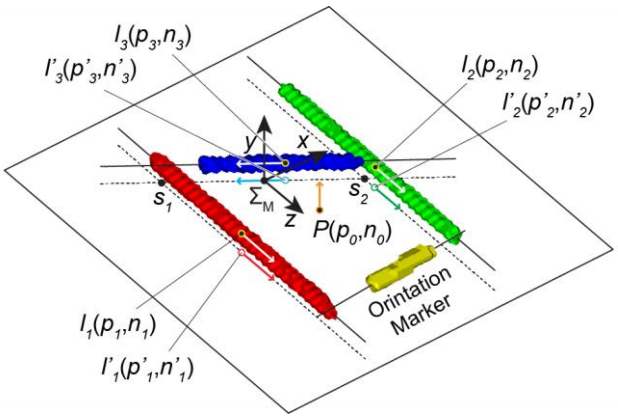

Figure 2: Marker segmentation and marker coordinate system

(Markers 1 and 2, Figure 2) are parallel to each other, defining a plane. For design convenience, the diagonal line marker (Marker 3) of the Z was placed slightly above the plane, but parallel to it (Figure 3a).

The Z shape of the markers is similar to that of Brown-Roberts-Wells stereotactic frames [18]. However, we only use one single Z structure and image-to-model registration over multiple image slices. The BRW frame is typically used with its special type of registration calculated on a single slice.

The first step of the registration is to segment the three linear markers in the images. A volume image is first reconstructed from the image series. For each line marker, a seed point corresponding to a region of the marker is then selected in the resliced images of the volume. The line marker region is segmented using a region growing algorithm. Finally, surface models of the markers are generated by applying a marching cube algorithm [19]. Figure 2 shows the surface models of the three segmented markers. Then, the centerlines of the markers are computed by applying a principal component analysis (PCA) and computing a centroid of the vertices, as shown in the figure. The three lines are $l_i(\vec{p}_i, \vec{n}_i), i = 1,2,3$, where $\vec{p}_i$ is a point on the line and $\vec{n}_i$ is its direction vector.

A coordinate system (Σ_M) is associated with the Z marker, located at the "center" of the Z structure, in the plane of the parallel markers (1 and 2). Since from the images the markers are not perfectly parallel, the plane $P(\vec{p}_0, \vec{n}_0)$ is estimated using both directions, as

$$\begin{aligned} \vec{p}_0 &= \tfrac{1}{2}(\vec{p}_1 + \vec{p}_2) \\ \vec{n}_0 &= \tfrac{1}{\|\vec{p}_1 - \vec{p}_2\|}(\vec{p}_1 - \vec{p}_2) \times \tfrac{1}{\|\vec{n}_1 + \vec{n}_2\|}(\vec{n}_1 + \vec{n}_2) \end{aligned} \quad \text{(Eq.1)}$$

where $\vec{p}_0$ is a point on the plane and $\vec{n}_0$ is a normal vector of the plane. All three lines are then projected onto the plane,

$$\begin{aligned} \vec{p}'_i &= \vec{p}_i - \left(\vec{n}_0 \cdot (\vec{p}_i - \vec{p}_0)\right)\vec{n}_0, i = 1,2,3 \\ \vec{n}'_i &= \vec{n}_i - (\vec{n}_0 \cdot \vec{n}_i)\vec{n}_0, i = 1,2,3 \end{aligned} \quad \text{(Eq.2)}$$

Then, the intersection points s_1 between l'_1 and l'_3 and s_2 between l'_2 and l'_3 are:

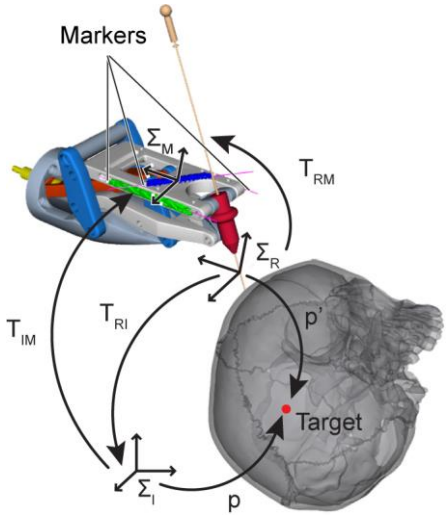

Figure 3: Schematic diagram of the image-to-robot registration

$$\begin{aligned} \vec{s}_1 &= \vec{p}_1 + a\vec{n}_1 = \vec{p}_3 + b\vec{n}_3, \{a, b \in \mathbb{R}\} \\ \vec{s}_2 &= \vec{p}_2 + c\vec{n}_2 = \vec{p}_3 + d\vec{n}_3, \{c, d \in \mathbb{R}\} \end{aligned} \quad \text{(Eq. 3)}$$

The center of the coordinate system is located centrally between s_1 and s_2, with the y direction normal to the P plane, and z direction aligned with the lateral markers, as shown in Figure 2. The corresponding transformation from the image space Σ_I to the marker space Σ_M is:

$$T_{IM} = \begin{bmatrix} \vec{x} & \vec{y} & \vec{z} & \vec{t} \\ 0 & 0 & 0 & 1 \end{bmatrix}$$

$$\text{where, } \begin{cases} \vec{x} = \vec{y} \times \vec{z} \\ \vec{y} = \vec{n}'_3 \times \vec{z} \\ \vec{z} = \frac{1}{\|\vec{n}'_1 + \vec{n}'_2\|}(\vec{n}'_1 + \vec{n}'_2) \\ \vec{t} = \frac{1}{2}(\vec{s}_1 + \vec{s}_2) \end{cases} \quad \text{(Eq.4)}$$

The robot coordinate system Σ_R is chosen at the RCM point of the RCM mechanism of the robot (Figure 3a), when the robot is at the position it was when the markers were imaged. In this position its location relative to the marker Σ_M is known from design, and the corresponding space transformation is T_{RM}.

Therefore, the robot to image registration is:

$$T_{RI} = T_{RM}\, {T_{IM}}^{-1} \quad \text{(Eq. 5)}$$

Figure 3 shows a schematic diagram of the image-to-robot registration. The transformation T_{RI} allows the transformation of any image target point p, to the robot space point:

$$p' = T_{RI} p \quad \text{(Eq. 6)}$$

Finally, the corresponding robot joint coordinates are calculated by solving the inverse kinematics of the robot, calculated based on the robot link parameters from the design.

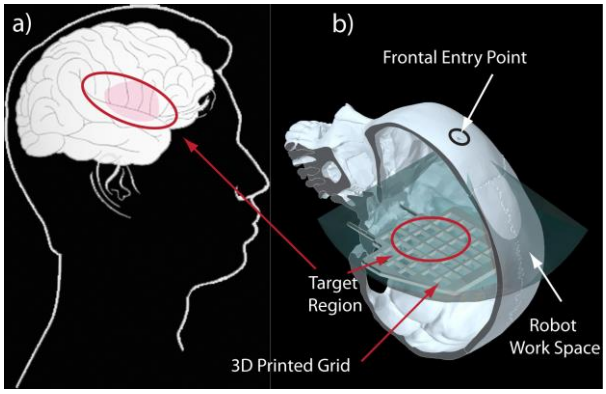

Figure 4: Skull Mockup with the grid of deep target

4. Direct MRI-Guided Targeting Tests

A series of tests were performed to test the accuracy of needle targeting. A mockup was designed to simulate the neurosurgical environment of procedures that require deep needle access such as biopsies, DBS (to tentorium cerebelli), and laser ablation of seizure foci. To these regions the depth of needle insertion from a frontal entry was estimated at approximately 100 mm.

A skull model (Functional Physiological Skeleton Model) was acquired. Computer Aided Design (CAD) software (Creo, PTC Inc.) was used to design a grid of 12 targets within the skull. This is a grid of rectangular bars that form several 10x10mm spaces, as shown in Figure 4. The grid was 3D printed (PLA, Makerbot Inc) and assembled in the designated position of the skull model. An appropriately located frontal entry point was selected and drilled in the skull. Then, the mockup was filled with gelatin, to simulate brain tissues. The gelatin was made of a 300 bloom gelatin powder (FX Warehouse Inc., Florida) in solution with sorbitol, glycerin, and water (3/3/2/25 parts by mass, respectively).

The centers of the gaps in the grid were considered as targets. Unlike using rigid targets, the hollow targets allowed the needle to be inserted all the way to the center, to better simulate the real scenario and facilitate accuracy measurements.

A ceramic 1.61mm diameter (slightly larger than 18Ga) needle with a symmetric point was built for the experiments, to eliminate possible artifact from the image and facilitate imaging the needle for targeitng accuracy measurements. A hollow ball made of plastic (ID:4.0 mm) was filled with Beekley MR contrast and precisely assembled at the top of the needle (Figure 6). The needle length to the ball center is 200 mm. This was subsequently used to measure the depth of needle insertion from the images.

The experiment was performed as follows:

1. The skull mockup was mounted on the head holder of the iMRIS table, and the robot was mounted and positioned so that the RCM point was at the skull entry hole.
2. An initial position of the robot was set and MR imaging coils were placed near the skull and robot.

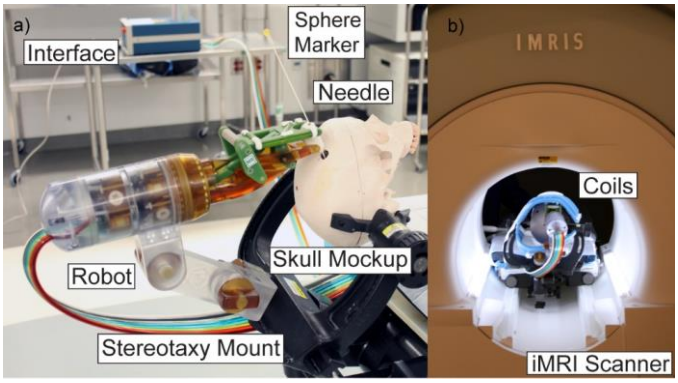

Figure 6: Robot and mockup a) on the table before docking the MR gantry and b) within the gantry.

3. MR images of the mockup and robot were acquired (T1/3D/1.5 Tesla, Number of images: 144, Field of view: 230.0×230.0×214.5mm, Image spacing: 0.898×0.898×1.50mm) and transferred to the registration computer via USB memory stick.
4. The robot was registered to the image space as described in Section 3.
5. Twelve target points of the grid were chosen for targeting based on the 3D reconstructed grid image (Figure 5).
6. Sequentially, the robot oriented the needle-guide and set the depth of needle insertion for each target.
7. The needle was inserted through the guide up to the marked depth. The insertion was performed manually by reaching within the scanner, without moving the gantry. The needle was spun by its shaft while inserting, to minimize the friction and reduce possible lateral defections [20]).

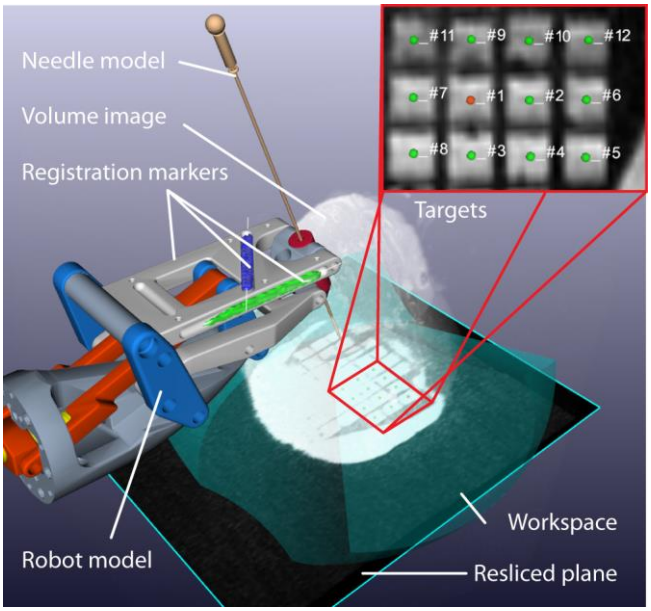

Figure 5: Virtual environment shown by the software and 12 target points at the centers of the grid gaps.

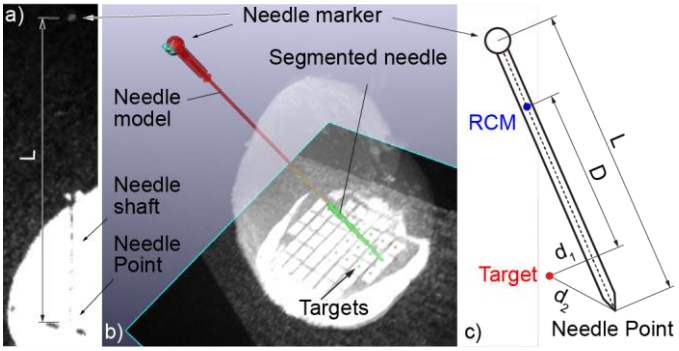

Figure 7: a) An image along the axis of an inserted needle shows that the needle point is difficult to locate along the gap made by the needle shaft. The ball marker at the top of the needle helps locating the point, with an offset L along the axis; b) 3D MRI image and segmented needle and targets; c) Needle targeting error measurement.

8. An image scan was performed after each insertion with the needle in the final position to verify targeting. The position of the needle was not in any way adjusted.

9. Steps 6 to 8 were repeated for each of the 12 targets.

The acquired images were processed after the procedure, as follows:

1. Reconstruct the series of MR images and build a volume image for each target.
2. Segment the needle and the needle marker from the reconstructed volume image, and compute the axis of the needle by applying principal component analysis and computing a centroid, in a similar manner to the marker registration.
3. Segment the ball marker at the needle top and find its centroid.
4. Register a 3D CAD model of the needle to the segmented needle by aligning the axes setting the depth based on the ball end marker.
5. Compute the target depth D as a distance between the RCM point of the robot and the target point in the direction of the CAD model needle (Figure 7).
6. Compute 2-dimensional (2D) targeting errors d_1 as the shortest distance between the target point and the CAD model needle axis.
7. Compute 3D errors d_2 as the shortest distance between the target point and the CAD model needle point.
8. Calculate targeting accuracy and precision as the average and standard deviation of the errors over all targets.

Table 1: Partial and total times for the experiment

Test Step		Time [min]
Robot and Mockup Mounting		5
Robot cable connection and Robot homing		6
Robot Positioning with RCM at the entry point		5
MR Coil Installation		3
MRI Scan for Registration		3
Image-Robot Registration		3
Total for Preparation , Registration		**25**
For each target	Target Selection	1
	Robot orientation of needle-guide and setting the depth of needle	0.5
	Manual needle insertion	1.5
	MRI scan for targeting error measurement	3
Total for 12 Targets		**72**
Total		**97**

Table 2: Direct MRI-Guided targeting errors

Target Number	Depth (D) [mm]	2D Error (d_1) [mm]	3D Error (d_2) [mm]
1	95.33	0.68	1.78
2	93.02	1.09	2.12
3	93.71	1.66	1.97
4	91.34	2.12	2.68
5	90.43	2.72	2.86
6	92.13	1.55	1.90
7	98.93	0.63	0.98
8	97.31	0.57	0.58
9	98.41	0.44	0.45
10	96.14	0.87	1.05
11	101.76	0.37	0.37
12	95.31	1.77	1.84
Max	101.76	2.72	2.86
Average (Accuracy)	95.32	1.21	1.55
StDev (Precision)	3.39	0.75	0.81
Accuracy $A_{(d)}$		$0.91 + 0.0031 \cdot d$	$1.25+ 0.0031 \cdot d$
Accuracy $A_{(76)}$		1.15	1.49

5. Results

Figure 7b shows the 12 target points on the grid, and a targeting example for target number 6, with the segmented needle, its axis, a segmented ball marker of the needle, and the registered CAD model of the needle.

The results of all targeting experiments and the overall accuracy and precision result are listed in Table 2. Based on the results at the average target depth of 95mm and the intrinsic robot errors ($A_{(d)} \approx A_{(0)} + e_R \cdot d$, $e_R = 0.0031$ [17]) the accuracy $A_{(d)}$ of needle targeting at a depth d is also shown in the table.

The experiment took 1.5 hours (Table 1), and no problems with robot functionality or image interference were observed.

6. Discussion and Conclusions

A feasibility study of in-scanner deep brain needle access under direct MRI guidance was performed. A recently reported MR Safe robot [17] was adapted for the procedure and used in the experiments. The previous report proved the MR compatibility of the robot and showed outstanding targeting accuracy in a Siemens scanner.

In the current experiments, among 12 targeting results, #5 showed the maximum error 2.72mm in 2D, 2.86 mm in 3D and #11 showed the minimum error 0.37 mm in 2D, 0.37 mm in 3D. The overall accuracy and precision at the mean target depth were 1.55mm and 0.81mm respectively, in 3D. 2D targeting results were slightly lower, showing that the O-ring depth setting is an effective way of setting the depth of needle insertion.

Based on the previous study, the 3D accuracy of targeting in the Siemens scanner calculated at the average depth (95.32mm) of the current targets is 1.88mm. The current value is slightly lower at 1.55mm, showing no compatibility problems with the iMRIS intraoperative scanner. The targeting error component related to imaging (3D) in the iMRIS was 1.25mm (Table 2), whereas in the Siemens Magnetom Aera was 1.59mm, similar values. Direct image quality comparison between the two scanners was not available.

We would like to point out the utility of the ball marker mounted at the end of the needle, which we have not used or seen used before. This has been very helpful to determine the depth of needle insertion (Figure 7a). The needle shaft is typically well visible within the images, but its point is difficult to identify precisely, especially for thin needles. Instead, the marker at the other end, which is filled with contrast, is easy to locate, therefore allowing the needle tip to be more accurately located by using an offset (L) along the needle axis. This may also explain the better accuracy results obtained in this study.

The overall targeting errors that we have measured at the needle point comprise multiple components, related to imaging, registration, manipulator errors, and needle insertion errors. Needle deflection errors are typically significant at deep targets. Still, robotic assistance enabled the needle point to be placed within 1.55mm of the point selected in the image. While in a phantom model, if it can be replicated in the clinical setting, this accuracy should be appropriate for most brain interventions. The simulated targets were placed very deep in the skull, so targeting at shallower depths will provide even better accuracy.

Other studies evaluating accuracy of stereotactic procedures for placement of intracranial instruments reported accuracies that are inferior to the accuracy obtained in our study [21-30]. The accuracy is increased by direct MR imaging as compared to pre-operative imaging [22, 31].

In our experiments, the guidance was performed fully robotically, and image-guided, without any trajectory correction. Similar MR robotic works in the field showed that corrections were needed to improve targeting [32]. Our mockup experiments show that accurate image guidance is possible from the first insertion, without the need for trial and error corrections.

Our needle insertion through the needle-guide was performed manually. In the experiments, we verified that with the iMRIS scanner it is possible to manually reach within the bore to insert the needle. Reaching the needle was not difficult, and it was possible to manipulate the needle softly, without disturbing the needle and the accuracy of targeting. Making a robot that fully positions the needle without the need for manual needle handling can be pursued in the future. However, in this first stage of development we opted to keep the surgeon in direct control of the needle.

The experiment shows the feasibility of accurately guiding slender instruments under direct MRI-guidance, all within the scanner. Without the robot, needle guidance and insertion at the scanner isocenter is difficult making direct visualization of the procedure impractical. Operations normally involve numerous in-out of the scanner moves between needle manipulation and subsequent imaging. With the robot and within a relatively short bore scanner, such as the iMRIS, it is now possible to perform procedures under direct image-guidance. The robot handles the guide and the physician inserts the needle while observing real-time images. Direct image feedback may prove useful for brain operations.

Time wise, as shown in Table 1, several robot preparatory steps can be performed concurrently with patient preparation, so these should not substantially contribute to the operative time. Then, actual targeting steps were fast, possibly helping to reduce overall operative time.

Based on the reported preclinical experiment the robot is sufficiently accurate for clinical applications. The size of the smallest clinically relevant target for implantation of a DBS electrode is the sub thalamic nucleus. Measurements of the subthalamic nucleus vary among studies and range from 20-105mm^3 as measured in MRI [33-35]. The corresponding radius range of spherical targets of these volumes is 1.68-2.92mm. The targets are very small, demanding high targeting accuracy. If placement is not accurate, the patients may present with speech and voice disorders, depression, and even in eye movement abnormalities. The 1.55mm reported accuracy is sufficient to target even the smallest 1.68mm radius target. Moreover, the shape to be targeted is not typically spherical. Richter et al, determined the anteroposterior length to be of 5.6 mm (3.4-9.7mm), the mediolateral length ranged from 2.5-5.3mm, and the average dorsoventral measurement was 5mm [33]. Therefore, the reported 1.55mm accuracy meets clinical requirements.

The depth of ~95mm of needle targeting in our experiments is also covering for the clinical case. DBS of the subthalamic nucleus is one of the deepest locations for placement of a DBS electrode. In a study [36], the distance from the entry point to the target measured in 10 patients undergoing DBS was found to be 76mm ± 8mm. Near 76mm depth, targeting accuracy is

1.49mm (Table 2), which is lower than the smallest clinically relevant target of 1.68mm.

If replicated clinically, the outstanding targeting accuracy with robot assistance could be an enabling technology for procedures such as deep-brain stimulation, laser ablation of epileptogenic foci and neoplasms, and other stereotactic procedures. By incorporating intraoperative MR imaging to the robotic system, we bypass the possibility of shift in intracranial structures after the dural opening. This avoids the risk of missing the targeted intracranial structure when using neuro-navigation systems that rely on pre-operative imaging.

Acknowledgments

The robotic technology utilized in the reported study was supported in part by awards 1R01CA172244 from the National Cancer Institute, RC1EB010936 from the National Institute of Biomedical Imaging and Bioengineering, and award W81XWH0810221 from the Department of Defense.

References

1. Li QH, Zamorano L, Pandya A, Perez R, Gong J, Diaz F: The application accuracy of the NeuroMate robot--A quantitative comparison with frameless and frame-based surgical localization systems. *Comput Aided Surg.* 2002; Vol.7(2) pp.90-98. PMCID:12112718
2. Glauser D, Fankhauser H, Epitaux M, Hefti JL, Jaccottet A: Neurosurgical robot Minerva: first results and current developments. *J Image Guid Surg.* 1995; Vol.1(5) pp.266-272. PMCID:9080346
3. Masamune K, Kobayashi E, Masutani Y, Suzuki M, Dohi T, Iseki H, Takakura K: Development of an MRI-compatible needle insertion manipulator for stereotactic neurosurgery. *J Image Guid Surg.* 1995; Vol.1(4) pp.242-248. PMCID:9079451
4. Comber DB, Barth EJ, Webster RJ: Design and control of an magnetic resonance compatible precision pneumatic active cannula robot. *Journal of Medical Devices.* 2014; Vol.8(1) pp.011003.
5. Davies B, Starkie S, Harris SJ, Agterhuis E, Paul V, Auer LM: Neurobot: A special-purpose robot for neurosurgery. 2000; Vol.4 pp.4103-4108.
6. Sutherland GR, Latour I, Greer AD: Integrating an image-guided robot with intraoperative MRI: a review of the design and construction of neuroArm. *IEEE Eng Med Biol Mag.* May-Jun 2008; Vol.27(3) pp.59-65. PMCID:18519183
7. Stoianovici D: Multi-Imager Compatible Actuation Principles in Surgical Robotics. *International Journal of Medical Robotics and Computer Assisted Surgery.* Jan 2005; Vol.1(2) pp.86-100. http://urobotics.urology.jhu.edu/pub/2005-stoianovici-MRCASJ.pdf. PMCID:17518382
8. Stoianovici D, Whitcomb LL, Anderson JH, Taylor RH, Kavoussi LR: A modular surgical robotic system for image guided percutaneous procedures. *Lecture Notes in Computer Science.* 1998; Vol.1496 pp.404-410. http://urobotics.urology.jhu.edu/pub/1998-stoianovici-miccai.pdf.
9. Taylor RH, Stoianovici D: Medical robotics in computer-integrated surgery. *IEEE Transactions on Robotics and Automation.* Oct 2003; Vol.19(5) pp.765-781. http://urobotics.urology.jhu.edu/pub/2003-taylor-ieeetra.pdf. PMCID:ISI:000185906400002
10. Stoianovici D, Cleary K, Patriciu A, Mazilu D, Stanimir A, Craciunoiu N, Watson V, Kavoussi LR: AcuBot: A Robot for Radiological Interventions. *IEEE Transactions on Robotics and Automation.* Oct 2003; Vol.19(5) pp.926-930. http://urobotics.urology.jhu.edu/pub/2003-stoianovici-ieeetra.pdf.
11. Li G, Su H, Cole GA, Shang W, Harrington K, Camilo A, Pilitsis JG, Fischer GS: Robotic system for MRI-guided stereotactic neurosurgery. *IEEE Trans Biomed Eng.* Apr 2015; Vol.62(4) pp.1077-1088. PMCID:25376035
12. Stoianovici D, Patriciu A, Mazilu D, Petrisor D, Kavoussi L: A New Type of Motor: Pneumatic Step Motor. *IEEE/ASME Transactions on Mechatronics.* Feb 1 2007; Vol.12(1) pp.98-106. ***2008 Best Paper Award of the Journal***. http://urobotics.urology.jhu.edu/pub/2007-stoianovici-tmech.pdf. PMCID:21528106
13. Patriciu A, Petrisor D, Muntener M, Mazilu D, Schar M, Stoianovici D: Automatic Brachytherapy Seed Placement under MRI Guidance. *IEEE Transactions on Biomedical Engineering.* Aug 2007; Vol.54(8) pp.1499-1506. http://urobotics.urology.jhu.edu/pub/2007-patriciu-tbme.pdf. PMCID:17694871
14. Stoianovici D, Kim C, Petrisor D, Jun C, Lim S, Ball MW, Ross AE, Macura K, Allaf ME: MR Safe Robot, FDA Clearance, Safety, and Feasibility of Prostate Biopsy Clinical Trial. *IEEE-ASME Transactions on Mechatronics.* Feb 2017; Vol.22(1) pp.115-126. http://urobotics.urology.jhu.edu/pub/2017-stoianovici-tmech.pdf
15. Stoianovici D, Kim C, Srimathveeravalli G, Sebrecht P, Petrisor D, Coleman J, Solomon SB, Hricak H: MRI-Safe Robot for Endorectal Prostate Biopsy. *IEEE-ASME Transactions on Mechatronics.* Aug 2014; Vol.19(4) pp.1289-1299. http://urobotics.urology.jhu.edu/pub/2014-stoianovici-tmech.pdf PMCID:4219418
16. Stoianovici D, Song D, Petrisor D, Ursu D, Mazilu D, Muntener M, Schar M, Patriciu A: "MRI Stealth" Robot for Prostate Interventions. *Minimally Invasive Therapy & Allied Technologies.* 2007; Vol.16(4) pp.241-248. http://urobotics.urology.jhu.edu/pub/2007-stoianovici-mitat.pdf. PMCID:17763098
17. Stoianovici D, Jun C, Lim S, Petrisor D, Monfaredi R, Wilson E, Krieger A, Fricke S, Sharma K, Cleary K: Multi-Imager Compatible, MR Safe, Remote Center of Motion Needle-Guide Robot. *IEEE Transactions on Biomedical Engineering.* Apr 25 2017; pp.Epub ahead of print. http://urobotics.urology.jhu.edu/pub/2017-stoianovici-tbme.pdf PMCID:28459678, 10.1109/TBME.2017.2697766
18. Heilbrun MP, Roberts TS, Apuzzo ML, Wells TH, Jr., Sabshin JK: Preliminary experience with Brown-Roberts-Wells (BRW) computerized tomography stereotaxic guidance system. *J Neurosurg.* Aug 1983; Vol.59(2) pp.217-222. PMCID:6345727
19. Cubes M: A High Resolution 3D Surface Construction Algorithm/William E. *Lorensen, Harvey E. Cline–SIG '87.* 1987.
20. Badaan S, Petrisor D, Kim C, Mozer P, Mazilu D, Gruionu L, Patriciu A, Cleary K, Stoianovici D: Does needle rotation improve lesion targeting? *International Journal of Medical Robotics and Computer Assisted Surgery.* Jun 2011; Vol.7(2) pp.138-147. http://urobotics.urology.jhu.edu/pub/2011-badaan-ijmrcas.pdf PMCID:PMC3100373;
21. Cardinale F, Cossu M, Castana L, Casaceli G, Schiariti MP, Miserocchi A, Fuschillo D, Moscato A, Caborni C, Arnulfo G, Lo Russo G: Stereoelectroencephalography: surgical methodology, safety, and stereotactic application accuracy in 500 procedures.

Neurosurgery. Mar 2013; Vol.72(3) pp.353-366; discussion 366. PMCID:23168681
22. Markowitz D, Lin D, Salas S, Kohn N, Schulder M: Compact Intraoperative MRI: Stereotactic Accuracy and Future Directions. *Stereotact Funct Neurosurg.* 2017; Vol.95(3) pp.197-204. PMCID:28614824
23. Bot M, van den Munckhof P, Bakay R, Stebbins G, Verhagen Metman L: Accuracy of Intraoperative Computed Tomography during Deep Brain Stimulation Procedures: Comparison with Postoperative Magnetic Resonance Imaging. *Stereotact Funct Neurosurg.* 2017; Vol.95(3) pp.183-188. PMCID:28601874
24. Chan AY, Tran DK, Gill AS, Hsu FP, Vadera S: Stereotactic robot-assisted MRI-guided laser thermal ablation of radiation necrosis in the posterior cranial fossa: technical note. *Neurosurg Focus.* Oct 2016; Vol.41(4) pp.E5. PMCID:27690660
25. Hunsche S, Sauner D, Majdoub FE, Neudorfer C, Poggenborg J, Gossmann A, Maarouf M: Intensity-based 2D 3D registration for lead localization in robot guided deep brain stimulation. *Phys Med Biol.* Mar 21 2017; Vol.62(6) pp.2417-2426. PMCID:28169225
26. Park SC, Lee CS, Kim SM, Choi EJ, Lee JK: Comparison of the Stereotactic Accuracies of Function-Guided Deep Brain Stimulation, Calculated Using Multitrack Target Locations Geometrically Inferred from Three-Dimensional Trajectory Rotations, and of Magnetic Resonance Imaging-Guided Deep Brain Stimulation and Outcomes. *World Neurosurg.* Feb 2017; Vol.98 pp.734-749 e737. PMCID:27876666
27. Pezeshkian P, DeSalles AA, Gorgulho A, Behnke E, McArthur D, Bari A: Accuracy of frame-based stereotactic magnetic resonance imaging vs frame-based stereotactic head computed tomography fused with recent magnetic resonance imaging for postimplantation deep brain stimulator lead localization. *Neurosurgery.* Dec 2011; Vol.69(6) pp.1299-1306. PMCID:21725253
28. Scheer JK, Hamelin T, Chang L, Lemkuil B, Carter BS, Chen CC: Real-time Magnetic Resonance Imaging-Guided Biopsy Using SmartFrame(R) Stereotaxis in the Setting of a Conventional Diagnostic Magnetic Resonance Imaging Suite. *Oper Neurosurg (Hagerstown).* Jun 01 2017; Vol.13(3) pp.329-337. PMCID:28521346
29. Tatsui CE, Nascimento CNG, Suki D, Amini B, Li J, Ghia AJ, Thomas JG, Stafford RJ, Rhines LD, Cata JP, Kumar AJ, Rao G: Image guidance based on MRI for spinal interstitial laser thermotherapy: technical aspects and accuracy. *J Neurosurg Spine.* May 2017; Vol.26(5) pp.605-612. PMCID:28186470
30. Vadera S, Chan A, Lo T, Gill A, Morenkova A, Phielipp NM, Hermanowicz N, Hsu FP: Frameless Stereotactic Robot-Assisted Subthalamic Nucleus Deep Brain Stimulation: Case Report. *World Neurosurg.* Jan 2017; Vol.97 pp.762 e711-762 e714. PMCID:26585721
31. Tanaka S, Puffer RC, Hoover JM, Goerss SJ, Haugen LM, McGee K, Parney IF: Increased frameless stereotactic accuracy with high-field intraoperative magnetic resonance imaging. *Neurosurgery.* Dec 2012; Vol.71(2 Suppl Operative) pp.ons321-327; discussion ons327-328. PMCID:22843131
32. Song S-E, Tuncali K, Tokuda J, Fedorov A, Penzkofer T, Fennessy F, Tempany C, Yoshimitsu K, Magill J, Hata N: Workflow assessment of 3T MRI-guided transperineal targeted prostate biopsy using a robotic needle guidance. 2014; pp.903612-903612-903616.
33. Richter EO, Hoque T, Halliday W, Lozano AM, Saint-Cyr JA: Determining the position and size of the subthalamic nucleus based on magnetic resonance imaging results in patients with advanced Parkinson disease. *J Neurosurg.* Mar 2004; Vol.100(3) pp.541-546. PMCID:15035292
34. Slavin KV, Thulborn KR, Wess C, Nersesyan H: Direct visualization of the human subthalamic nucleus with 3T MR imaging. *AJNR Am J Neuroradiol.* Jan 2006; Vol.27(1) pp.80-84. PMCID:16418362
35. Zwirner J, Mobius D, Bechmann I, Arendt T, Hoffmann KT, Jager C, Lobsien D, Mobius R, Planitzer U, Winkler D, Morawski M, Hammer N: Subthalamic nucleus volumes are highly consistent but decrease age-dependently-a combined magnetic resonance imaging and stereology approach in humans. *Hum Brain Mapp.* Feb 2017; Vol.38(2) pp.909-922. PMCID:27726278
36. York MK, Wilde EA, Simpson R, Jankovic J: Relationship between neuropsychological outcome and DBS surgical trajectory and electrode location. *J Neurol Sci.* Dec 15 2009; Vol.287(1-2) pp.159-171. PMCID:19767016

Changhan Jun received a B.S. degree from the Department of Mechanical, Materials and Aerospace Engineering, Illinois Institute of Technology, Chicago, IL, USA in 2010. He received a M.S. degree at the Department of Mechanical Engineering, Johns Hopkins University, Baltimore, MD, USA in 2013. Since 2012, he studies toward a Ph.D. degree at Urology Robotics Laboratory, Johns Hopkins University, Baltimore, MD, USA. His research interests include image-guided robots and medical devices.

Sunghwan Lim received a B.S. degree from the Department of Mechanical Engineering and Materials Science, Yokohama National University, and a M.S degree from the Department of Bioengineering, The University of Tokyo, Japan, in 2008 and 2010, respectively. From 2010 to 2012, he was an Instructor at the Gondar Polytechnic College, Ethiopia. From 2012 to 2014 he was Research Scientist at the Biomedical Research Institute, Korea Institute of Science and Technology, Seoul, Korea. He is currently working toward a Ph.D. degree at The Johns Hopkins University, Baltimore, MD, USA. His research interests include image-guided medical robots and medical imaging.

Jean-Paul Wolinsky received his MD from Baylor College of Medicine where he also completed his training in neurosurgery. He also trained in neurosurgical oncology at the MD Anderson Cancer Hospital. He completed a fellowship in spine surgery and oncology at the Johns Hopkins Hospital, and subsequently became Professor and Clinical Director of the Carnegie Center for Surgical innovation at Johns Hopkins. Since 2017, Dr. Wolinsky is Professor of Neurosurgery at the Northwestern University School of Medicine. He has published over 200 peer reviewed articles, extensively lectured nationally and internationally, and is a member of numerous professional organizations.

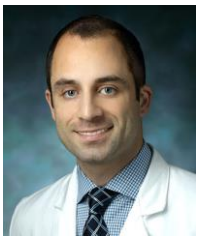

Tomas Garzon-Muvdi graduated from medical school from the Universidad Autonoma de San Luis Potosi, obtained a Masters in Science degree from Wright State University in Neurophysiology and Biophysics, and was a post-doctoral fellow in the Johns Hopkins Hospital brain tumor stem cell laboratory from 2008 to 2011. He is currently chief resident in the Neurosurgery Department at Johns Hopkins Hospital. Dr. Garzon-Muvdi is interested in applying new technologies to improve the care and outcomes of neurosurgical patients. This includes applications of robotic technology, augmented reality, and intraoperative imaging technologies. His research interests also include mechanisms that glioblastoma utilizes to elude the immune system.

Doru Petrisor received a MS degree in Mechanical Engineering from the University of Craiova, Romania in 1988, the PhD from the University of Petrosani, Romania in 2002, followed by a research fellowship in Urology at the Johns Hopkins University. Between 1991-1994 he was Assistant Professor at the University of Craiova and Lecturer since 1994. In 2002 he joined the Urology Robotics research group at Johns Hopkins and currently is Research Associate Professor. Dr. Petrisor's specialty is design and manufacturing of medical devices. His bibliography includes numerous articles, presentations, and 4 patents of invention.

Kevin Cleary received a BS and MS degree in Mechanical Engineering from Duke University in 1982 and 1983, followed by a PhD from the University of Texas in 1990. He is a Professor of Radiology and Pediatrics at George Washington University. At Children's National Medical Center, he is the director of the Bioengineering Initative, where he works with his clinical partners to bring technology to assist in pediatric care. His main interests include medical robotics, rehabilitation robotics, and biomedical devices.

Dan Stoianovici received the Ph.D. degree from Southern Methodist University, Dallas, TX, in 1996. He is Professor of Urology, Mechanical Engineering, Neurosurgery, and Oncology at the Johns Hopkins University. He is also the Director of the Robotics Program. His specialty is medical robotics in particular robotic hardware and image-guided robots. His bibliography includes numerous publications and 22 patents of invention. He serves on the editorial boards of the IEEE/ASME TRANSACTIONS on Mechatronics, Journal of Endourology, International Journal of Medical Robotics and Computer Aided Surgery and other cross disciplinary medical-engineering journals.